J Mater Sci

Electronic materials

Multiscale characterisation of the electrical response of 3d printed carbon black polylactic acid

Delbart Robin[1], Noble Thomas[2], Roumy Laurane[3], Fernandez Toribio Juan Carlos[4], Robert Colin[2], Truong Hoang Thuy Quynh[5], and Martinez Hergueta Francisca[1,*]

[1] *Institute for Infrastructure and Environment, School of Engineering, University of Edinburgh, Edinburgh, UK*
[2] *Institute for Materials and Processes, School of Engineering, University of Edinburgh, Edinburgh, UK*
[3] *Institut PPRIME, Dpt Physique et Mecanique des Materiaux, CNRS-ENSMA-Universite de Poitiers, Poitiers, France*
[4] *Materials Innovation Factory, University of Liverpool, Liverpool, UK*
[5] *ESTACA, Pôle Mécanique des Structures Composites et Environment, Ecole d'ingénieurs, Laval, France*

Received: 3 May 2023
Accepted: 5 August 2023

ABSTRACT

In this paper, the electrical response of a carbon black polylactic acid 3D printed polymer is characterised in detail by a combination of advanced experimental techniques at different scale lengths. The electrical properties as a function of the temperature become repeatable after the second heating cycle, exhibiting different trends as a function of the printing parameters. Joule heating and oven-heating techniques have been compared, showing the advantages of the Joule heating method to maintain electrical conductivity due to the lower thermal inertia. Small-Angle X-Ray Scattering has been employed to discern the underlying physics, showing the crucial role of crystallinity, filler dispersion and carbon black aggregates to form an effective segregated conductive network. This investigation provides guidelines to produce 3D-printed devices with a reliable electrical response and the governing equations to operate them with sufficient accuracy for engineering applications.

Handling editor: Maude Jimenez.

Address correspondence to E-mail: francisca.mhergueta@ed.ac.uk

https://doi.org/10.1007/s10853-023-08840-6
Published online: 19 August 2023

Springer

GRAPHICAL ABSTRACT

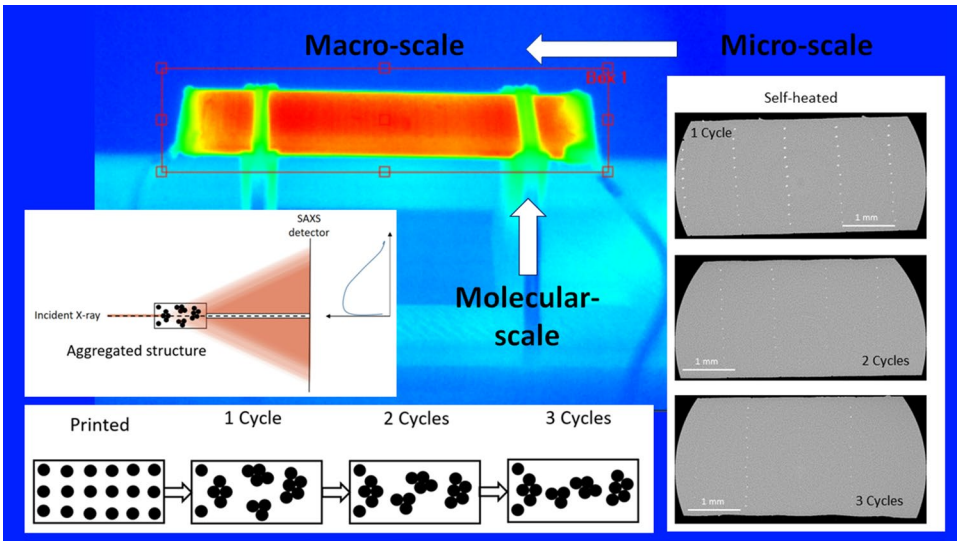

Introduction

4D printing is an emerging Additive Manufacturing technique to produce bespoke Shape Memory Polymers triggered by external stimuli such as water, heat or pressure [1]. Heat-sensitive Shape Memory Polymers can be programmed by inducing internal stresses that are released once the device is heated above the glass transition temperature, creating a temporary actuator [2–5]. 4D printed actuators are lightweight, low-cost and relatively simple in comparison to conventional pneumatic, electro-mechanical or electromagnetic actuators [6, 7]. They could be potentially implemented in a wide range of applications, such as the deployment of solar arrays [8, 9], soft robotics [10, 11], intravascular and trachea stents [12–14], reflector antennas [15, 16] or tissue engineering [17, 18]. Since the technologies reported in the literature depend on external stimuli, the reliability of these devices for engineering applications is currently a hot topic [19–21]. For instance, large deployed structures might present substantial temperature gradients that will cause difficulties during the simultaneous operation of multiple actuators distributed along the structure [22].

One approach to control these temperature gradients is the in-situ printing of electrical circuits that could heat the actuator by Joule effect [23–26]. Electrical circuits are conventionally embedded in structural components by 3D printing to successfully manufacture sensors, flexible circuits and wearable devices [27–30]. They employ conductive filaments based on conventional polymers such as Polylactic acid (PLA) filled with metal particles, carbon black, graphene or carbon nanotubes [27, 31–35]. These filaments offer several applications such as electrode materials [36], impedimetric sensors [37] or wearable devices [38]. Since they are mainly employed to conduct electricity at low voltages, the information available in the literature regarding their thermoelectric response is limited. For low applied voltages (below 6 V), the electrical resistivity is a unique value conventionally employed to calculate the intensity of the circuit [39]. However, for high applied voltages, Joule's effect increases the temperature of the material resulting in an increase in resistivity which might follow a different trend depending on the microstructure of the multifunctional polymer [40]. In particular, above the glass transition temperature, multifunctional polymers experience drastic changes in mechanical [41, 42] and electrical properties including resistivity [43, 44], which is critical for the development of Joule heated 4D printing. Additionally, the strong anisotropy of material properties in 3D printed samples also needs to be considered since the characteristic mesostructure (composed of a repeatable sequence of filaments and voids) influences the electrical performance [45]. In summary, further efforts are required to characterise the thermoelectric governing relationships between resistivity and temperature of 3D printed multifunctional polymers in order to transform Joule heated

4D printing into a reliable technology for engineering applications.

Few authors have reported studies in electrical characterisation of 3D printed multifunctional particle reinforced polymers [39, 40, 46]. These studies focused on the characterisation of thermoelectrical properties from a phenomenological point of view. They reported changes in resistivity with temperature, finding different trends for each experimental campaign despite using the same commercial material since they employed different equipment and printing parameters. The differences between those studies could be explained by shedding light on the fundamental physics behind the non-linear thermoelectric trends observed, using advanced characterisation techniques. The previous studies disregarded the role of printing parameters, void content and 3D printed mesostructure, crystallinity and carbon particle aggregation at molecular level, mechanisms that couple to define the global non-linear themoelectric trends observed [47, 48]. This knowledge could be employed to unify the outcomes in the reported literature and set a common direction for the future design of 3D printed electrical components based on carbon fillers.

This study aims to investigate the electrical response of a multifunctional 3D printed carbon black reinforced PLA composite as a function of the printing parameters and the heating technique. In order to do that, advanced experimental techniques at different length scales have been used to determine the macroscopic degradation of resistivity with temperature, the evolution of electrical properties due to thermal cycles, the crystallinity (Differential Scanning Calorimetry), the microstructure evolution of porosity (X-ray micro-computed tomography) and the filler dispersion (Small Angle X-Ray scattering). The experimental results have been combined, analysed and discussed to discern the fundamental physics governing the thermoelectric response.

Materials & methods

Materials & manufacturing

The material selected for this study is a multifunctional Polylactic Acid (PLA) filament charged with carbon black (CB) particles. It is supplied by the company Protoplant and commercialised under the brand name Proto-Pasta. According to the datasheet, the polymer blend contains 65 W% Natureworks 4043 PLA reinforced with an average carbon black particle content of 21.43 W% and 12. 7 W% of an unknown polymer [40]. The coupons were produced by a Prusa i3 MK3S FDM printer. The printing parameters were selected considering a previous investigation in mechanical characterisation [42]. A 1 mm diameter nozzle was chosen at 100% extrusion ratio, one perimeter layer and a fixed deposition velocity of 45 mm/s. The temperature of the nozzle and the printing bed were set as 225 °C and 60 °C respectively. The dimensions of the specimens were 15 x 70 mm and 2.4 mm in thickness. Two different raster directions, 0 ° and 90 °, parallel and perpendicular to the loading direction were selected to determine the influence of the mesostructure in the thermoelectric performance. In addition, the influence of the layer height was analysed, with samples printed at 0.05, 0.1 and 0.2 mm. The samples were wired by applying conductive silver paint at the edges, with wires attached with Araldite to minimize contact resistance.

Thermal characterisation

The thermal properties were determined by Differential Scanning Calorimetry (DSC). The characterisation was conducted using a PerkinElmer DSC 8000 in nitrogen atmosphere. The specimen temperature was stabilised at 30 °C for 5 min and then heated up to 220 °C at a constant rate of 10 °C/min. This analysis provided the thermogram curves (heat flow as a function of temperature) to identify the glass transition, the cold crystallisation and the melting temperatures. The degree of crystallinity was calculated according to [49]:

$$X_c = \frac{1}{w}\frac{\Delta H_m - \Delta H_c}{\Delta H_m^0}, \tag{1}$$

where ΔH_m and ΔH_c are the enthalpies of fusion and cold recrystallisation of the specimen respectively and ΔH_m^0 is the enthalpy of fusion for 100% crystalline PLA, taken from the literature as 93 J/g [50]. w stands for the PLA mass fraction obtained from the datasheet and normalises the result considering the percentage of carbon black particles in the material [51].

The thermal expansion coefficient was measured with a DIL 402 Expedis Classic dilatometer. The specimens were 3D printed with 5 mm thickness and 0.1 mm layer height, and small cube samples of dimensions 5 x 5 x 5 mm^3 were extracted with a

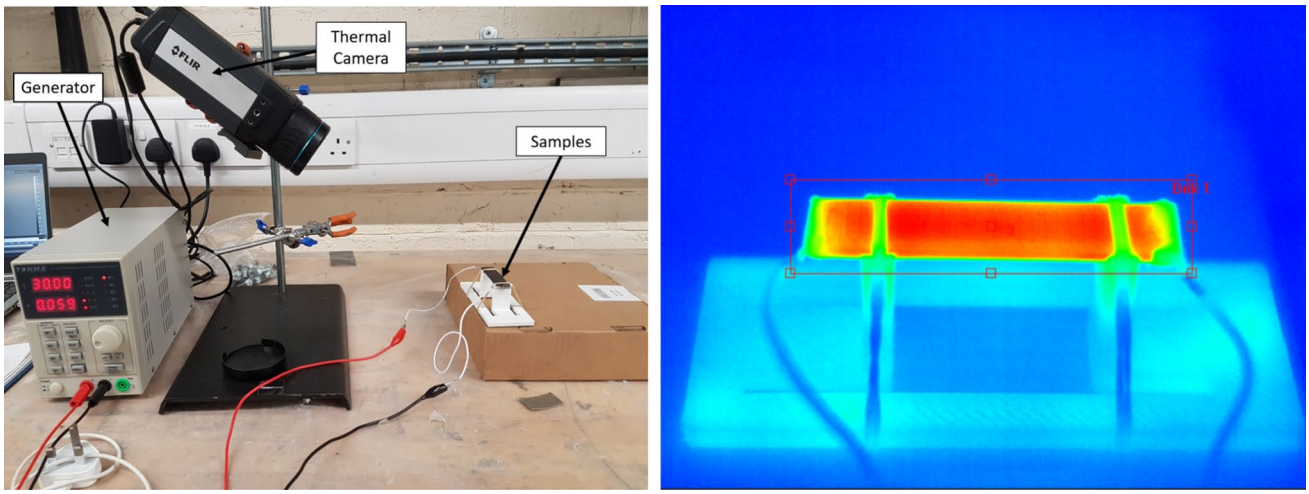

Figure 1 Experimental set-up for the Joule heating method (left picture), and temperature field recorded by the thermal camera (right picture).

Mecatome T210 Presi cutting machine, ensuring all the faces of the samples were parallel. Two samples were tested for each configuration to ensure the reproducibility. The thermal expansion coefficient was measured along the filament direction up to 120 °C with a heating rate of 1 °C/min and a load cell of 0.001 N. Two subsequent heating cycles were performed to determine the differences in thermal expansion coefficient before and after annealing and to understand the influence of the residual stresses generated during the manufacturing process.

Thermoelectrical characterisation

Joule heating

To analyse the Joule heating response, a potential difference of 30 V (DC current) was applied to the specimens with a TENMA 72-2540 generator. Considering the dimensions of the specimens, 5 min were enough to stabilise the resistance and temperature values. The thermal cycles were composed of 3 heating steps with a 6 min cooling step (enough time for the sample to cool at room temperature) between each cycle. The samples were fixed on a classic 3D printed PLA test bench and were attached thanks to two rubber bands. The resistance was registered with the generator, meanwhile temperature distributions were monitored with a FLIR A655SC thermal camera, see Fig. 1.

Oven heating

The influence of an external heat source in the thermoelectric response of the material was conducted employing a SciQuip oven-230HT. The samples were first heated up to 50 °C at 5 °C/min heating rate. The temperature was then progressively increased in steps of 5 °C, and maintained for 5 min to induce a homogeneous temperature over the sample. The temperature of the sample was monitored by three taped thermocouples equally distributed along the specimen to register temperature gradients. The evolution of the resistance was registered with a TENMA 72-2540 generator employing a low potential difference of 15 V, avoiding any undesirable Joule heating. Thermal cycles were also performed, extracting the samples from the oven for 6 min to allow them to return to room temperature.

Data treatment

The evolution of thermoelectric properties was quantified by the fractional change in resistance ($\Delta R/R_0$), computed according to equation (2):

$$\Delta R/R_0 = \frac{R_i - R_0}{R_0} * 100 \tag{2}$$

where R_i stands for the monitored resistance and R_0 stands for the initial resistance at room temperature. To guarantee the statistical significance of the experimental results, 5 repetitions of each test were carried

out and the mean values and standard deviations were calculated.

Microscale morphological characterisation

X-ray micro computed tomography

X-ray micro computed tomography (microCT) was employed to determine the evolution of the meso-structure under thermal cycling loading. The tomograms were obtained with a in-house instrument available at The School of Geoscience of The University of Edinburgh. The instrument comprises (i) a Feinfocus 10-160 keV dual transmission and reflection X-ray source, (ii) a Micos 160-Air ultra-high precision air-bearing rotary sample table and (iii) a Perkin Elmer XRD0822 amorphous silicon flat panel X-ray camera with a terbium-doped gadolinium oxysulfide scintillator, with 20 x 20 cm size and 1 megapixel resolution. 967 radiographs were registered for each tomogram using an exposure time of 2.5 s, and tomograms were reconstructed using a filtered back-projection algorithm implemented within the reconstruction software Octopus v8.9. The reconstructed volume encompassed an area of 25 mm^2 with a resolution of 4.88 μm/voxel. The tomograms were post-processed using a Python script to determine the ratio between void and material pixels. Each measurement employed 906 slices perpendicular to the filament direction.

Small-angle x-ray scattering

SAXS was employed to characterise the evolution of the filler dispersion with the thermal cycles [52–54]. SAXS measurements were performed by a nanostar SAXS equipment from Bruker. The X-ray beam wavelength provided was $\lambda = 1.3642$ Å and the measurements were calibrated with an AgBh (silver behenate) substrate. All measurements were carried out in a vacuum with an exposure time of 20 min. The scattering pattern was collected by a CDD detector using a sample-to-detector distance of 2070 mm. The final pattern was spatially corrected to obtain a flat 2D image. The scattering patterns were postprocessed using the software Diffrac.SAXS from Bruker. Azimuthal integrations were computed to obtain the averaged intensity values as a function of the q-spacing. Kratky plots were computed as well, where an extra factor q^2 was multiplied by the scattering intensity [55]. The

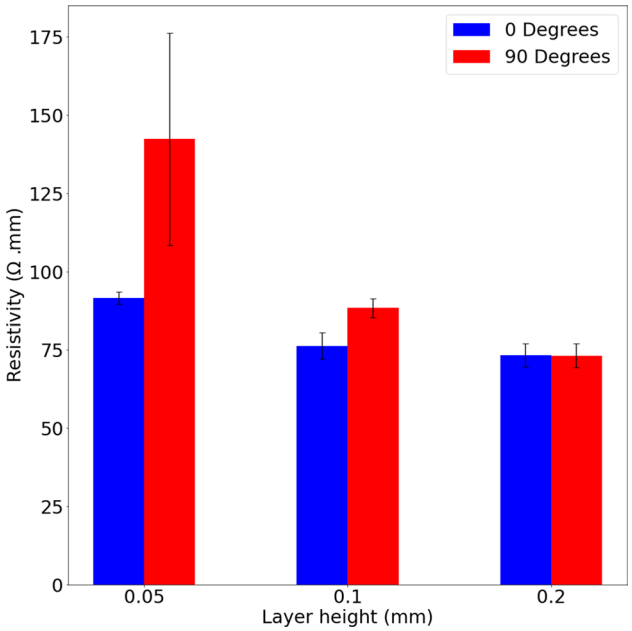

Figure 2 Initial resistivity as a function of the layer height and the raster direction.

average size of the primary particles and the mass fractal aggregates was estimated by fitting the SAXS intensity curves to the Beaucage Unified Power model [56] using the software SasView [57–59]. Two different levels were employed to estimate the two different radius of gyration (R_g). The q range was divided into two areas, at the crossover point between the scattering regimes, and the fitting procedure was conducted in two steps. First, the high-q range was fitted to determine the average primary particle size, and afterwards, the second level was fitted within the q range 0.02 to 0.1 Å, to estimate the average radius of gyration of the mass fractal aggregates.

Result

Baseline thermal and electrical properties

The resistivity of the printed specimens as a function of the layer height and the raster direction is plot in Fig 2. The best conductivity is obtained for the thicker layer height of 0.2 mm, with similar behaviour regardless of the raster direction. A progressive increment in resistivity is observed when decreasing the layer height, in particular for the raster direction 90 °. The specimens printed at raster direction 0° exhibit a limit increment of resistivity, from 73.29 to 91.47 $\Omega \cdot mm$ of

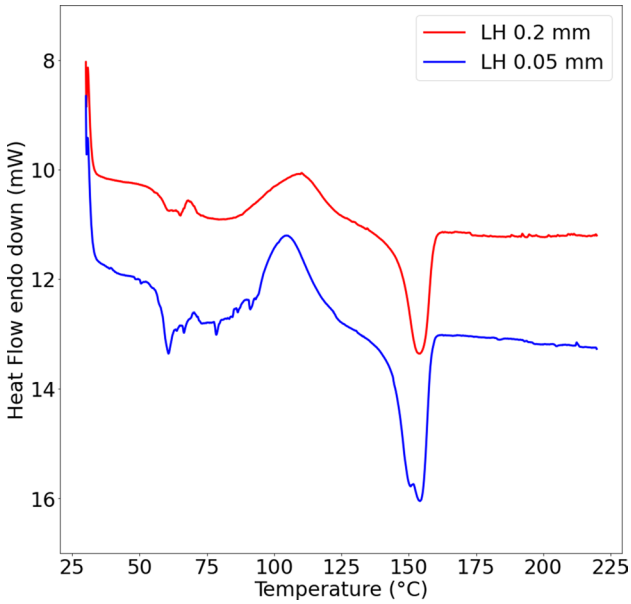

Figure 3 Heat flow endo down for samples after being printed with a layer height of 0.2 mm and 0.05 mm.

resistivity when decreasing the layer height from 0.2 to 0.05 mm. The specimens at raster direction 90° instead present a dramatic loss of conductivity and a large increment of scattering for low layer heights, reaching $142.26\,\Omega \cdot mm$ for 0.05 mm.

Figure 3 shows the DSC thermograms of the 3D printed samples. Three characteristic temperatures can be distinguished: (i) the glass transition temperature, T_g, between 48°C and 60°C, (ii) the cold crystallisation exotherm peak, T_c, between 70°C and 120°C and (iii) the melting peak, T_m, between 153°C and 155°C. The crystallisation rate has been calculated according to equation 1 and provides a degree of crystallinity of 2.80% and 15.78% for the 0.05 mm and 0.2 mm layer heights respectively.

The thermal expansion coefficient as a function of the temperature is shown in figure 4. The first cycle corresponds to the first heating after being printed, and the second cycle is the repetition of the experiment after the sample has been cooled. During the first heating cycle, the thermal coefficient does not follow the characteristic response of PLA [60] and presents a negative expansion coefficient once the temperature approaches the T_g. Several anomalous negative and positive peaks are registered as a consequence of the internal stresses induced by the 3D printing process [61, 62]. This phenomenon is a result of the change in viscosity according to the temperature. A sudden drop in the thermal expansion coefficient occurs at 48 °C, reaching a maximum negative value of -0.0017^oC^{-1} at a temperature of 54.1 °C. The response becomes unstable after a second peak is developed with a maximum positive value of 0.0012^oC^{-1} at 81.6 °C. After this annealing process, the thermal coefficient stabilises. During the second cycle, a different behaviour is observed. The thermal expansion coefficient increases quickly until the T_g. Afterwards, the rate of increment slows down until reaching an absolute maximum at 77 °C.

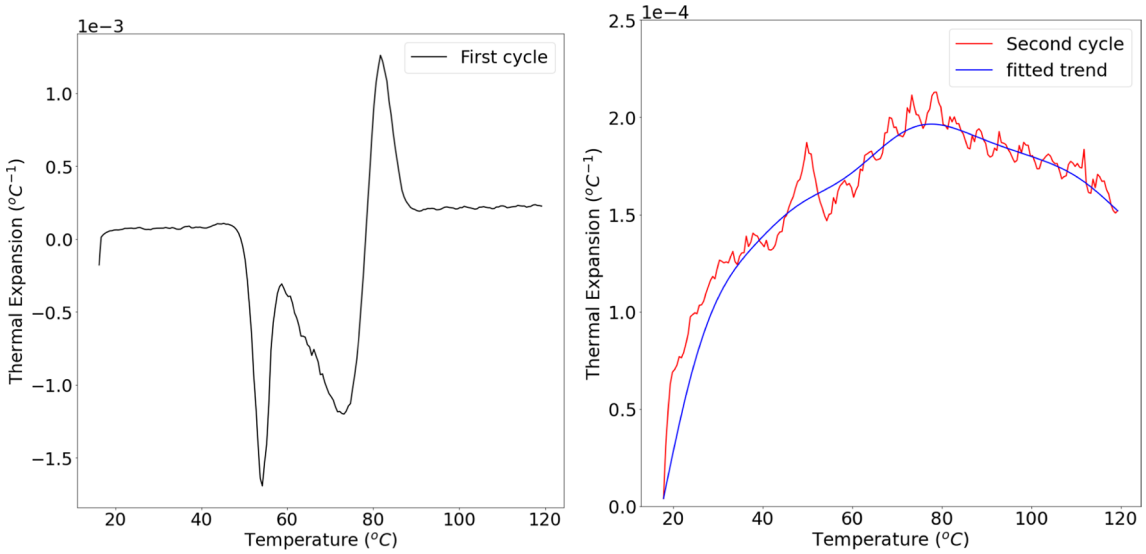

Figure 4 Thermal expansion coefficient as a function of the temperature after being printed (left side) and after annealing (right side).

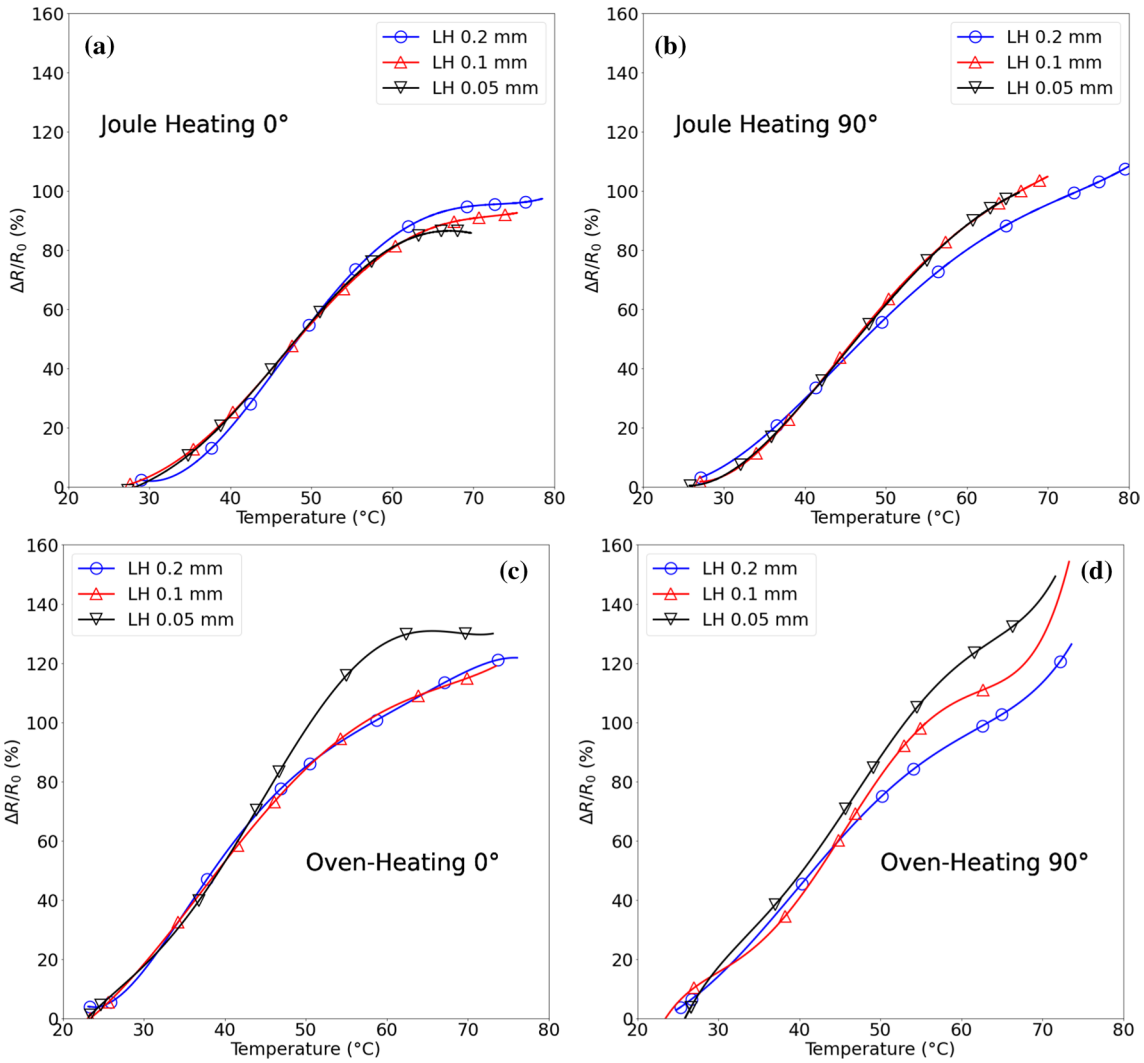

Figure 5 Representative curves of the fractional change in resistance (%) of the Joule heated and oven-heated samples printed at 0° (**a** and **c**) & 90° (**b** and **d**).

Thermo-electric characterisation

Figure 5 shows a summary of the representative curves of the evolution of the percentage of resistance amplitude (RA) as a function of the temperature for the different configurations and heating techniques. In all cases, an increment of resistivity with temperature is registered, showing a degradation of the electrical properties at high temperatures, characteristic of multifunctional particle-reinforced polymers [63]. All the configurations present a reliable response below the glass transition temperature (T_g), and a change in trend above the T_g, with different responses as a function of the raster direction and heating method. The Joule heated samples printed at 0°, see Fig. 5a, present replicable evolution of resistance regardless of the layer height. In addition, the resistance stabilises after 65 °C. On the other hand, the Joule heated samples at raster direction 90°, see Fig. 5b, show a deviation of the samples printed with 0.2 mm layer height, and a further increase in resistivity above the T_g. In comparison, the oven-heating technique induces a faster degradation of electrical properties than the Joule heated counterpart, and a higher variability of the electrical response. Significant differences as a function of the layer height are registered for samples printed at 0°, see Fig. 5c, with a large increase in resistance for a layer height 0.05 mm, and a posterior stabilisation above T_g. All the rest of the configurations present a progressive degradation of

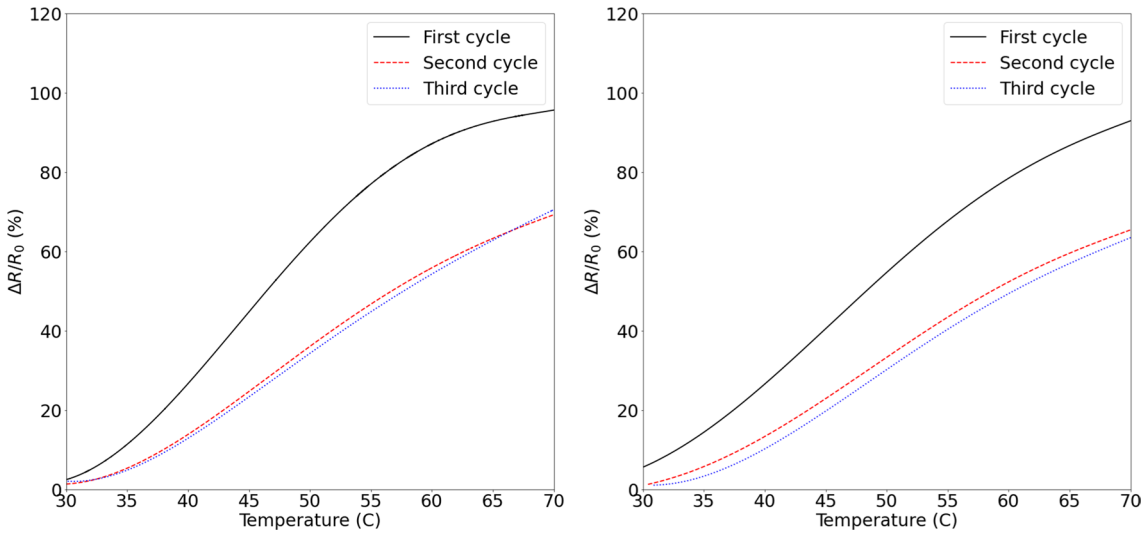

Figure 6 Fractional change in resistance due to thermal Joule heating cycles for the samples printed with a layer height of 0.2 mm at 0° (left side) and 90° (right side) raster angles.

electrical properties above T_g during oven-heating, with particularly large increments of resistance for samples printed at 90°, see Fig. 5d.

Thermal cycles

Thermal cycles imposed by different heating techniques have been investigated to analyse the influence of thermal inertia on the reliability of the electrical properties. Both methods applied the same temperatures on the specimens, however, each technique resulted in a different heating rate, with the Joule's heating samples warming faster. Figure 6 illustrates the fractional change in resistance of samples subjected up to three thermal Joule heated cycles for the layer height of 0.2 mm printed at 0° (left side) and 90° (right side). R_0 is updated for each new cycle with the initial resistance value at room temperature. The electrical behaviour during the first cycle (black full line) exhibits higher degradation of electrical properties than the subsequent second (red dash line) and third cycles (blue round dotted line), which present a replicable thermoelectric response with negligible changes in trends within the range analysed. These results are comparable with previous measurements registered for bulk polymers reinforced with carbon black particles [64]. Similar results are obtained for the remaining layer heights.

Figure 7 plots the initial resistivity values for each Joule heating cycle. The same trends are registered for mean values and associated scattering regardless of the raster direction and the layer height. The differences between the subsequent cycles have no statistical significance, although an initial degradation of electrical properties is registered after the first heating cycle, followed by a slight improvement in resistivity after the second cycle, in particular for the samples printed at raster direction 0°.

Microscale characterisation

A microscale characterisation of the samples printed at 0° was conducted to determine the main heat and electronic transfer micromechanisms. First of all, the thermal cycles induce a different evolution of the degree of crystallinity as a function of the layer height, see Fig. 8. The samples printed at 0.2 mm layer height present a constant degree of crystallinity (with an average value of 15.9%) regardless of the heating technique and the number of cycles. This degree of crystallinity is considered the maximum achievable by this polymer blend due to the poor crystallisation ability of conventional PLA under atmospheric pressure [65]. On the other hand, the samples printed with a 0.05 mm layer height suffer cold recrystallisation as a result of the annealing imposed during the thermal cycles when heated above 70°C. This increment in the degree of crystallinity is proportional to the imposed thermal inertia [66], and is in agreement with the longer time duration needed to heat the samples in the oven (30 min) vs the Joule

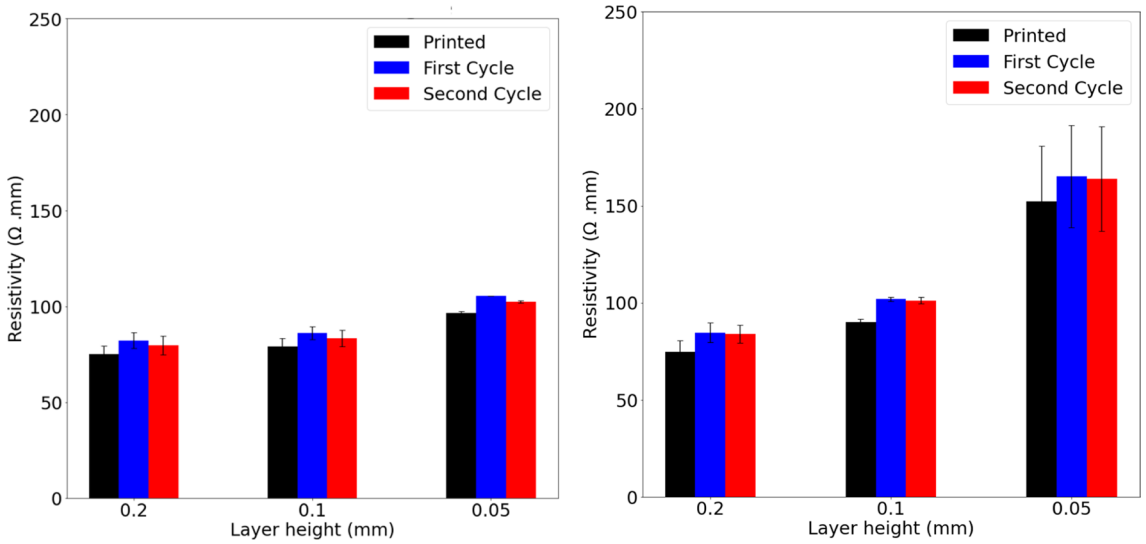

Figure 7 Initial resistivity of thermally Joule heated cycled samples printed at 0° on the left and 90° on the right.

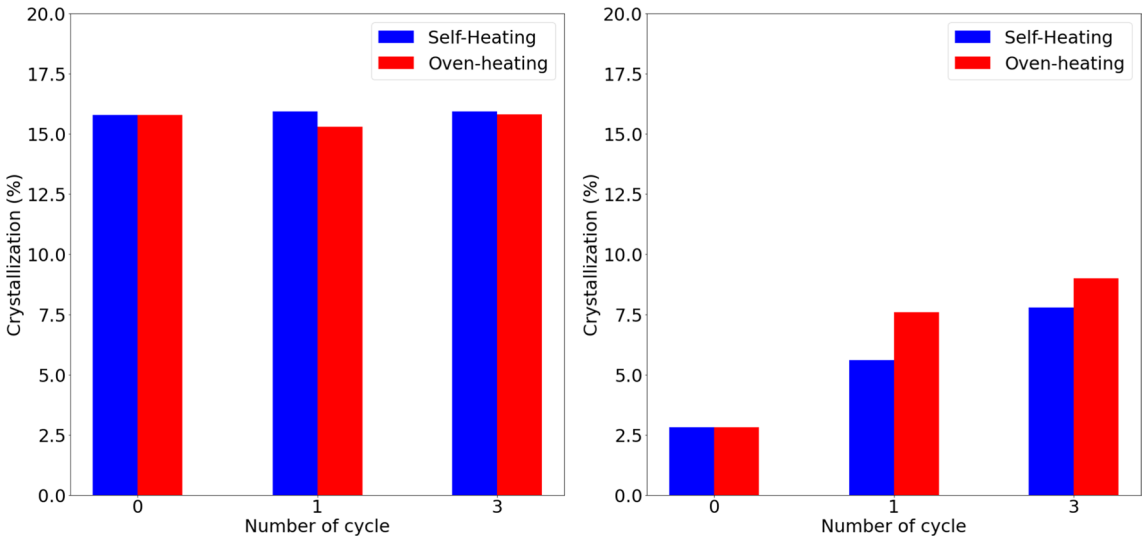

Figure 8 Evolution of the crystallinity as a function of the thermal cycles for specimens printed with a layer height of 0.2 mm (left) and 0.05 mm (right).

heating technique (5 min instead), showing a higher increment of the degree of crystallinity for the oven-heated samples.

Further analysis of the evolution of the microstructure was conducted by micro CT scan. Figure 9 shows representative tomographies of the baseline printed samples with layer height 0.2 mm, and the evolution of porosity for different heating methods. Figure 10 summarises the results, quantifying the ratio between void and material pixels. Different trends in the evolution of porosity are registered as a function of the heating technique. Oven-heated samples tend to decrease the void content progressively, meanwhile, the Joule heating technique induces a drastic increment of the porosity with the first heating cycle, and reduces the porosity progressively afterwards. The large increment of porosity for the first Joule heating thermal cycle correlates with the initial negative thermal expansion coefficient registered before the samples have been annealed, see Fig. 4. The release of the internal stresses (induced during 3D printing) retracts the material leading to an increase in void

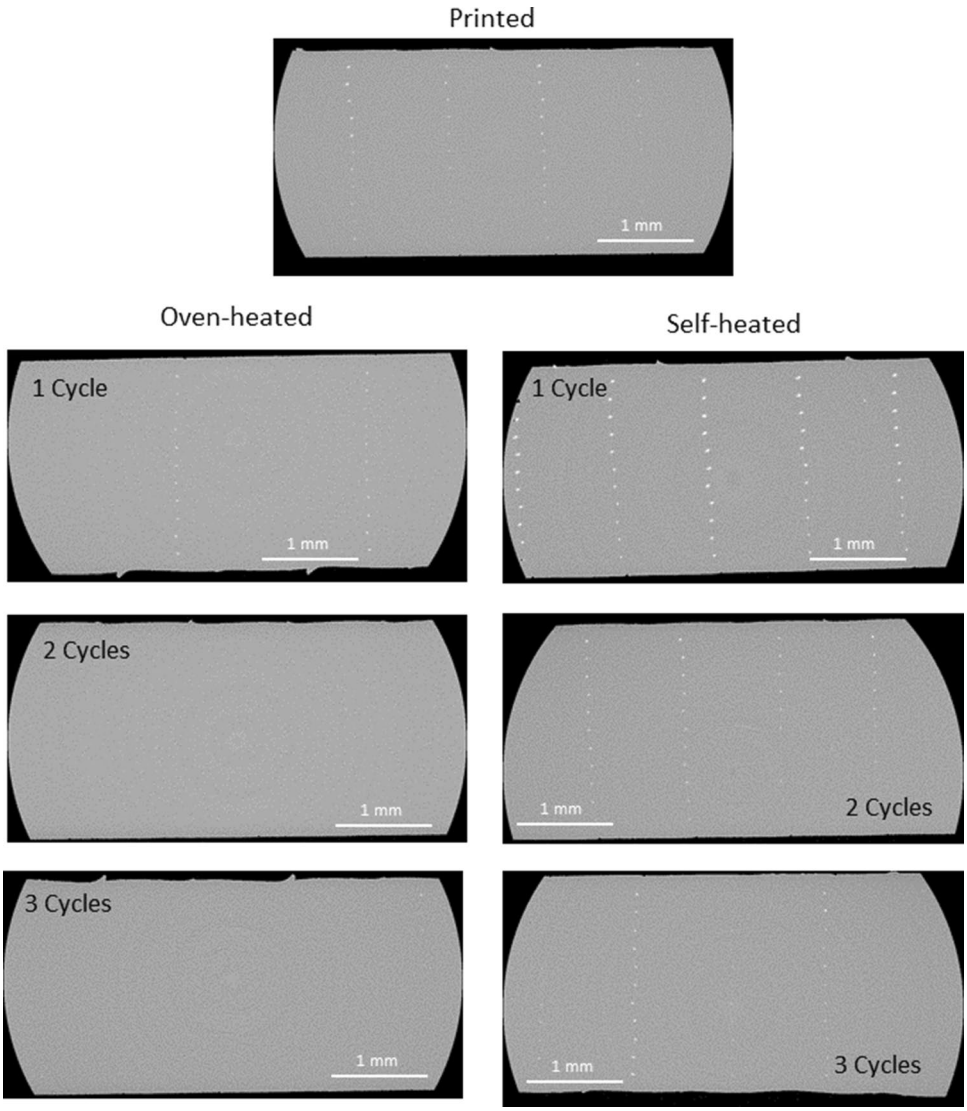

Figure 9 Representative tomographies of 3D printed samples printed at 0 with a layer height of 0.2 mm. Baseline printed sample at the top, and thermally cycled samples by oven heating (left side) and Joule heating (right side).

content. After the second Joule heating cycle, since the material is heated above the T_g, the PLA polymer is fully annealed and all the internal stresses have been released, the polymer flows through the weldlines and reduces the void content progressively similar to the oven-heated technique.

The filler distribution at the nanoscale has been investigated by SAXS. Figure 11 compares the intensity curves and the Kratky plots of the printed samples with layer heights 0.05 and 0.2 mm. Two different regions can be distinguished: (i) the outer region at high q-values, representative of the surface scattering by primary particles and (ii) the intermediate q-spacing scattering produced by mass fractal aggregates [67]. The initial scattering peak is an instrumental artefact of the SAXS device. Both configurations present a similar trend at high q-spacing up to a value $q_{si} = 0.065$ Å^{-1}, the crossover point between the scattering regimes. This is representative of a carbon black particle size $d_{si} =$ 96Å, where $d_{si} = \frac{2\pi}{q_{si}}$. This q region was adjusted with a Beaucage Unified Power fit with a radius of gyration $R_g = 43.57$ Å. Assuming a spherical particle, $\phi = 2R_g\sqrt{\frac{5}{3}}$, this corresponds to a particle size of 112.5 Å, very close to the initial particle size estimated from the crossover point and in agreement with the values and scattering reported in [67].

In the intermediate region, each configuration presents a different trend. The sample printed with 0.05 mm layer height shows uniform sizes distribution of mass fractal aggregates, between

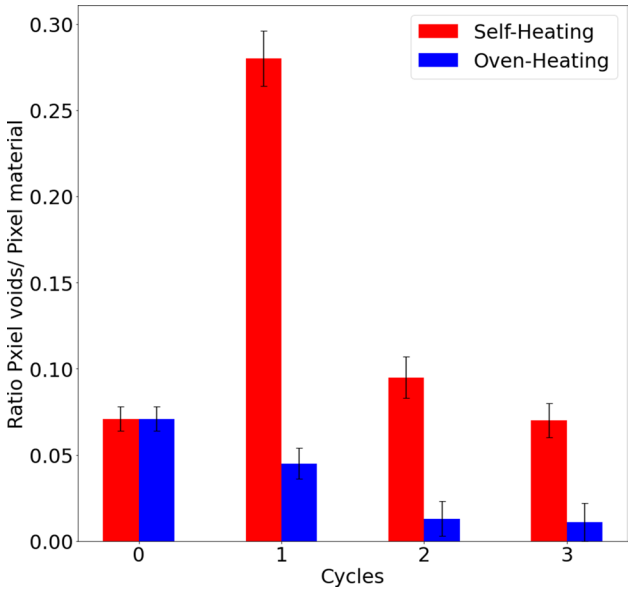

Figure 10 Ratio between void and material pixels for micro CT tomographies.

q_{agg} = 0.025 Å^{-1} and q_{agg}= 0.065 Å^{-1}. On the other hand, the sample printed with 0.2 mm layer height presents a pronounced hump, representative of mass fractal aggregates of similar size on average R_g = 161.68 Å. Since aggregates tend to migrate to the boundaries of polymer crystals, this statistical difference correlates with the higher degree of crystallinity of this configuration [68–70]. Furthermore, since this sample possesses lower initial resistivity, see Fig. 2, these particular mass fractal aggregates seem to benefit the electrical properties of the material.

Figure 12 shows the evolution of the Kratky plots for the thermal cycles, as a function of the layer height (0.2 and 0.05 mm) and the heating method (oven-heating and Joule heating). The thermal cycles impose a different filler migration depending on the heating technique and the evolution of crystallinity. The samples printed with 0.2 mm layer height do not present a noticeable dynamic aggregation while Joule heated, see Fig. 8a, indicating negligible changes to the segregated conductive network. In the oven-heated case, the slope of the hump is reduced, showing the development of new aggregates and agglomerates with a large variety of sizes, see Fig. 8b. The samples printed with 0.05 mm layer height instead progressively increase the crystallinity with the thermal cycles, see Fig. 8b, providing preference locations for primary CB particles to segregate. As a result, the CB particles migrate into the new crystal boundaries, generating new mass fractal aggregates with a preferential average size registered by pronounced humps in the SAXS curves, see Fig. 12c and d. No noticeable dynamic aggregation is registered after the first heating cycle from a SAXS perspective.

Discussion

The raster direction is the first relevant parameter to consider in the electric response of 3D printed samples. The samples printed at orientation 0° exhibit a response representative of the original multifunctional polymer, however, using a printing direction orthogonal to the electric path might increase artificially the resistivity depending on the weldlines between adjacent filaments. Fig 13 shows the differences in weldlines for samples printed at raster direction 90° and layer heights of 0.2, 0.1 and 0.05 mm. The electrical resistivity registered in Fig. 2 is directly proportional to the extension of the fractured area, which increases with the layer height. In the case of the thickest layer height (0.2 mm, see Fig. 13a), weldlines (highlighted in red) are consistently formed at each layer, resulting in negligible disruption to the electric path. This indicates that the characteristics of the segregated conductive network of the 0.2 mm layer height samples are equivalent for both raster directions. Nevertheless, for thinner layer heights, the experimental width of printing is lower than the theoretical value, hence weldlines are not formed on each layer, see Fig. 13c. As a result, large voids appear randomly in the samples, disrupting the electrical path and leading to poor electrical properties, lower repeatability, and a larger standard deviation. These findings are consistent with previous studies on the characterization of 3D printed components, which have highlighted the critical role of interface continuity in the mechanical response of such components, prioritizing it over porosity considerations [42]. Based on these consistent observations, we can infer that the continuity of the interfaces enhances electrical properties by establishing a more consistent and evenly distributed conductive network.

The second parameter to consider is the layer height. Higher layer heights (e.g. 0.2 mm) exhibit lower resistivity and better electrical performance, see Fig. 2. The electrical properties of multifunctional polymers are highly sensitive to the gap width of the quantum

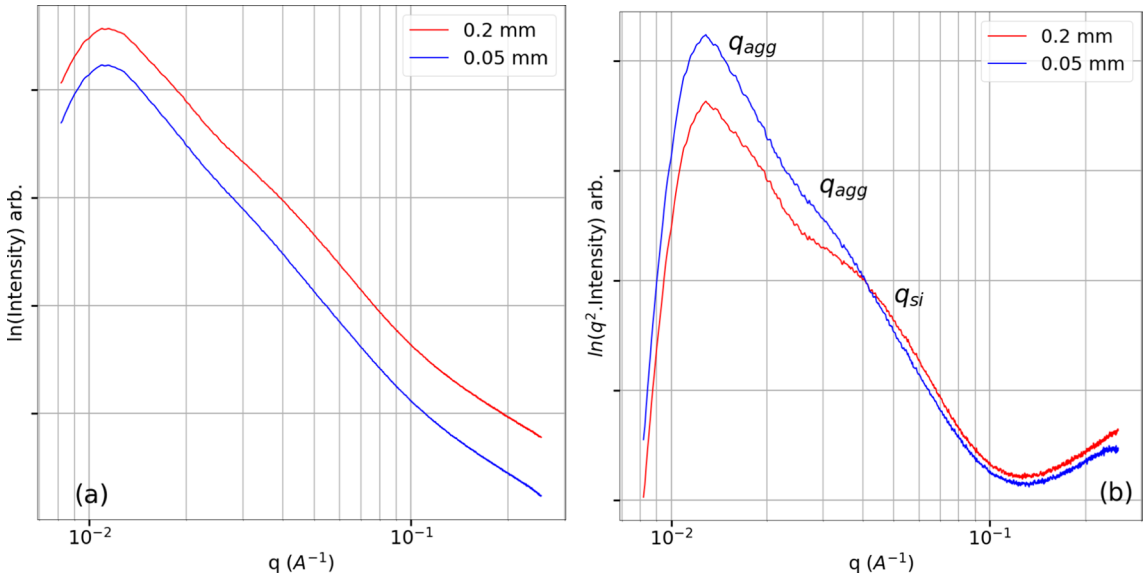

Figure 11 SAXS intensity curves **a** and Kratky plot **b** of samples printed at a layer height of 0.2 mm and 0.05 mm.

tunnelling effect (defined by the conductive particles) and the interparticle distance, proportional to the particle diameter [71]. As such, molecular networks with homogeneously distributed particle aggregates can provide continuous electron paths that cannot be established by isolated large agglomerates. Comparing the distribution of aggregates characterised by SAXS for different configurations, see Fig. 11, and the initial crystallinity of the 3D printed samples, see Fig. 8, it can be concluded that the improved electrical performance of the samples printed with layer height 0.2 mm is a result of the higher percentage of mass fractal particle aggregates of a particular size, probably distributed along the crystal boundaries. This seems to play a critical role in the electric performance of the material, leading to an improved segregated conductive network and lower resistivity.

In any case, the increment in temperature has a detrimental impact on the electrical properties of the multifunctional polymer. All the configurations present an increase of resistivity with temperature, see Fig. 5. The thermal energy supplied during the heating process provides additional mobility to the CB particles, deteriorating the conductive network [72]. Since the oven-heating technique provides a higher thermal inertia than the Joule heating technique, it results in a higher increment of resistivity. The effect of high temperatures is even more detrimental in the case of the samples printed with a raster angle of 90°, showing a major disruption of the segregated conductive network formed by discrete adjacent filaments.

The evolution of resistivity with cyclic thermal loading was driven by a series of competing mechanisms that results in different responses at different scales. At the molecular scale, the thermal inertia (i) increases the degree of crystallinity of the PLA matrix and (ii) migrates CB particles into thermodynamically stable positions. The boundaries of the PLA crystals offer a stable location for CB small aggregates, see Fig. 12c and d, resulting in an effective segregated conductive network. However, in our study, this mechanism is limited by the maximum degree of crystallinity of the PLA blend, around 15%. Once this mechanism is exhausted, if additional thermal energy is supplied to the system, particles and small aggregates will continue to migrate towards more thermodynamically stable positions, clustering in large agglomerates and deteriorating the conductive network [73], see Fig. 12b. CB particle migration seems to be limited to the first heating cycle, with no perceptible differences in particle distribution for subsequent cycles that do not overtake the maximum previous temperature. As such, no additional deterioration of the electric properties is registered, see Fig. 6.

At the macroscale, resistivity is driven by the changes in the 3D printed architecture. The differences in resistivity between cycles for the Joule heated specimens, see Fig. 7, correlates with

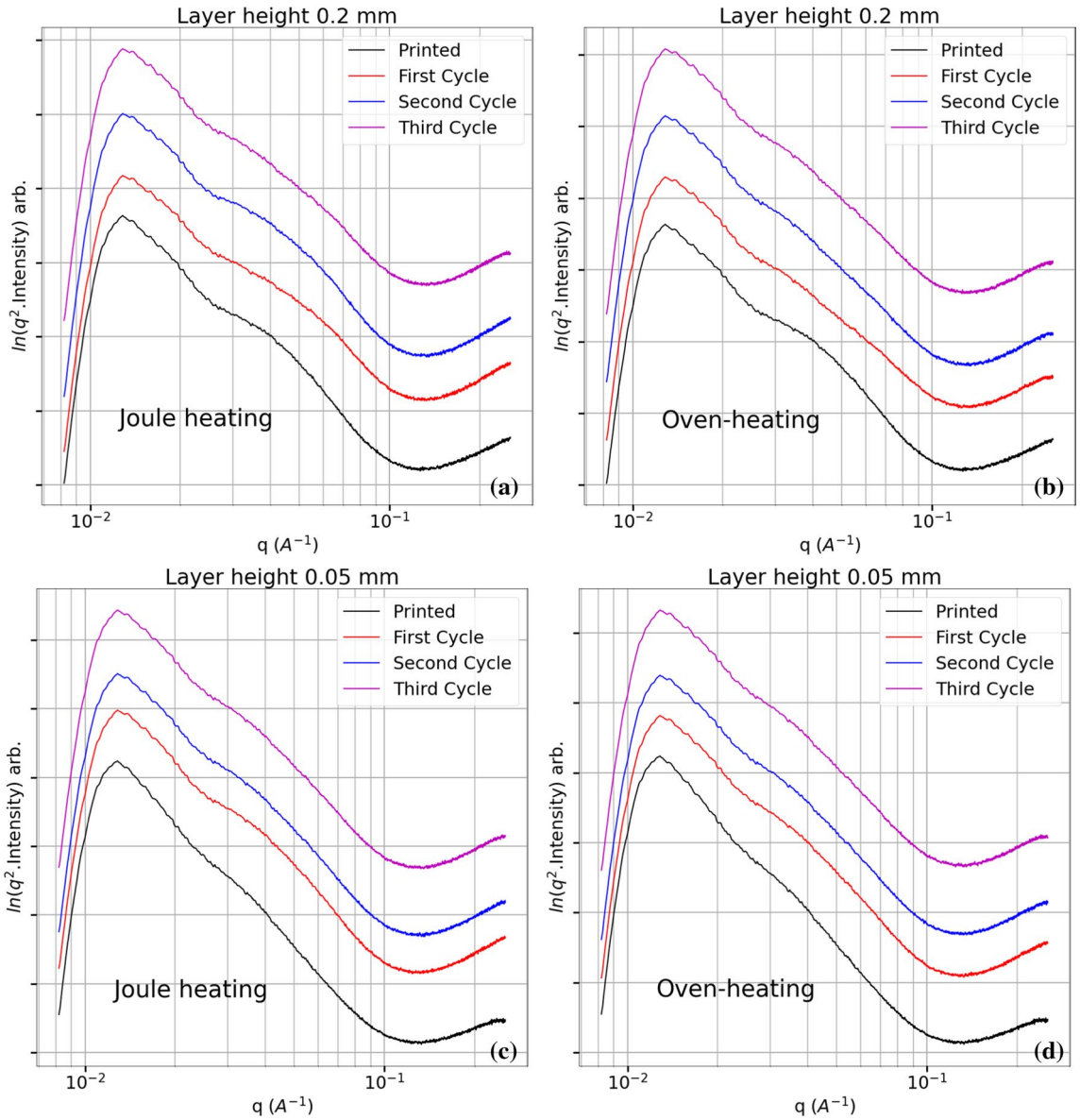

Figure 12 Kratky plot of samples printed at a layer height of 0.2 mm (**a** and **b**) and 0.05 mm (**c** and **d**) and Joule heated (left side) or oven-heated (right side).

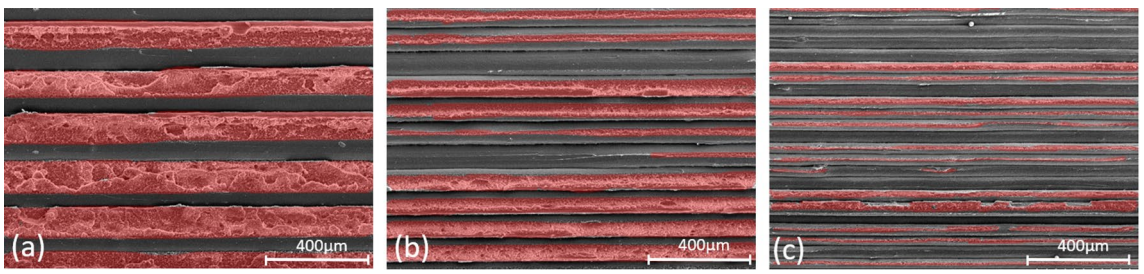

Figure 13 SEM pictures of broken samples printed at 90°- with a layer height of 0.2 mm **a**, 0.1 mm **b** and 0.05 mm **c**. Weldlines are highlighted in red.

the evolution of porosity, see Fig. 10. The first Joule heating cycle results in an increment in porosity that overall increases the resistivity of the specimens. The remaining cycles instead show a slight improvement in electrical performance, justified by (i) the decrease in void content registered by the CT-Scan and (ii) the limited thermal inertia induced by Joule heating, which cannot activate the detrimental migration of the CB mass fractal aggregates into large agglomerates.

Conclusion

The electrical response of a 3D printed carbon black reinforced PLA polymer has been analysed in detail by means of a combination of experiments carried out at different length scales. The thermoelectric response has been determined for different cyclic thermal loads, providing the relationship between resistance and temperature, useful for design applications and discerning the fundamental physics responsible for the phenomena.

The macroscopic tests show that the initial resistivity is highly influenced by printing parameters such as the raster direction and the layer height. For instance, the samples printed parallel to the electric path present superior electric performance and reliability, being representative of the overall response of the multifunctional polymer. On the other hand, samples printed with a raster direction perpendicular to the electric path exhibit poor electric performance due to the lack of consistent welding between adjacent filaments, in particular for thin layer heights. The layer height also has an impact on the initial resistivity of the material due to differences in filler distribution at the microscale level. The samples printed with the thickest layer height (0.2 mm) present a high percentage of mass fractal aggregates that play a critical role in the connectivity of the segregated conductive network, resulting in an improved electric path.

The resistivity of the multifunctional polymer increases with the temperature as a result of the molecular particle mobility. No perceptible deterioration of the electric properties is registered for subsequent thermal cycles that do not overtake the maximum previous temperature, however, a slight improvement in electric performance can be obtained when the void content decreases as a result of the polymer flow and additional welding of the filaments above the glass transition temperature.

Large differences in electrical response are registered for the oven-heating and the Joule heating techniques as a result of the different thermal inertia induced. The oven-heating method, with higher thermal inertia, releases the internal stresses originated during 3D printing and allows the polymer to flow and weld the filaments, decreasing progressively the void content. At a molecular scale, it accelerates the increment of the degree of crystallinity, and migrates the CB particles to mass fractal aggregates located at the crystal boundaries, or large agglomerates once that mechanism becomes saturated. The Joule heating technique instead imposes a lower thermal inertia. As a result, additional thermal cycles are requested to release the internal stresses produced during 3D printing. At a molecular level, the Joule heating technique minimises the increment of crystallinity and limits particle migration, maintaining the original segregated conductive network and preserving the multifunctional properties of the material.

This investigation provides the basis to manufacture 3D-printed devices with reliable thermoelectric properties. An improved and repeatable response can be programmed if devices are (i) printed at a raster direction following the electric path, (ii) printed with thicker layer heights and (iii) subjected to an initial Joule heating cycle above the maximum expected in-service temperature. This investigation unlocks the design of technologies such as Joule heated 4D printing for industrial applications and provides the thermoelectric laws to operate devices with sufficient accuracy.

Acknowledgements

This research is sponsored by the Defense Science and Technology Laboratory (DSTL) (grant number DSTLX1000144021R). The support of the Henry Royce Institute through the Royce PhD Equipment Access Scheme enabling access to the Small-Angle X-Ray Scattering facilities at The University of Liverpool (EPSRC Grant Number EP/R00661X/1) is gratefully acknowledged. For the purpose of open access, the authors have applied a Creative Commons Attribution (CC BY) licence to any Author Accepted Manuscript version arising from this submission.

Author contributions

RD contributed to Investigation, methodology, formal analysis, software, visualisation, data curation, validation, writing—Original draft preparation. TN contributed to Methodology, writing—review and editing. LR contributed to Investigation, writing—review and editing. JCT contributed to Investigation, formal analysis, writing—review and editing. CR contributed to Investigation, methodology, supervision, writing—review and editing. QTH contributed to supervision, conceptualisation, funding acquisition, writing—review and editing. FMH contributed to supervision, conceptualisation, funding acquisition, writing—Original draft preparation.

Data availability

The data will be shared upon request.

Declarations

Conflict of interest The authors have no conflicts of interest to declare. All co-authors have seen and agree with the contents of the manuscript and there are no known competing financial interests or personal relationships that could have appeared to influence the work reported in this paper.

Ethical approval Not applicable

References

[1] Momeni F, Liu X, Ni J et al (2017) A review of 4d printing. Mater Des 122:42–79

[2] Ge Q, Qi HJ, Dunn ML (2013) Active materials by four-dimension printing. Appl Phys Lett 103(13):131901

[3] Wu J, Yuan C, Ding Z, Isakov M, Mao Y, Wang T, Dunn ML, Qi HJ (2016) Multi-shape active composites by 3d printing of digital shape memory polymers. Sci Rep 6(1):1–11

[4] Yuan C, Wang T, Dunn ML, Qi HJ (2017) 3d printed active origami with complicated folding patterns. Int J Precis Eng Manuf Green Technol 4(3):281–289

[5] Subash A, Kandasubramanian B (2020) 4d printing of shape memory polymers. Eur Polym J 134:109771

[6] Schniederjans DG (2017) Adoption of 3d-printing technologies in manufacturing: a survey analysis. Int J Prod Econ 183:287–298

[7] Rafiee M, Farahani RD, Therriault D (2020) Multi-material 3d and 4d printing: a survey. Adv Sci 7(12):1902307

[8] Barrett R, Taylor R, Keller P, Lake M, Stern T, Freebury G, Beidleman N (2007) Design of a solar array to meet the standard bus specification for operation responsive space. In: 48th AIAA/ASME/ASCE/AHS/ASC Structures, Structural Dynamics, and Materials Conference, p. 2332

[9] Campbell D, Barrett R, Lake MS, Adams L, Abramson E, Scherbarthn M, Welsh JS, Freebury G, Beidleman N, Abbot J (2006) Development of a novel, passively deployed roll-out solar array. In: 2006 IEEE Aerospace Conference, p. 9. IEEE

[10] Zolfagharian A, Kaynak A, Kouzani A (2020) Closed-loop 4d-printed soft robots. Mater Des 188:108411

[11] Hongying Z (2018) Development of topology optimized 3d printed soft grippers and dielectric soft sensors

[12] Agarwal T, Hann SY, Chiesa I, Cui H, Celikkin N, Micalizzi S, Barbetta A, Costantini M, Esworthy T, Zhang LG et al (2021) 4d printing in biomedical applications: emerging trends and technologies. J Mater Chem B 9(37):7608–7632

[13] Kim Y, Yuk H, Zhao R, Chester SA, Zhao X (2018) Printing ferromagnetic domains for untethered fast-transforming soft materials. Nature 558(7709):274–279

[14] Zarek M, Mansour N, Shapira S, Cohn D (2017) 4d printing of shape memory-based personalized endoluminal medical devices. Macromol Rapid Commun 38(2):1600628

[15] Liu Y, Du H, Liu L, Leng J (2014) Shape memory polymers and their composites in aerospace applications: a review. Smart Mater Struct 23(2):023001
[16] Im E, Thomson M, Fang H, Pearson J, Moore J, Lin J (2007) Prospects of large deployable reflector antennas for a new generation of geostationary doppler weather radar satellites. In: AIAA SPACE 2007 Conference & Exposition, p. 9917
[17] Murphy SV, Atala A (2014) 3d bioprinting of tissues and organs. Nat Biotechnol 32(8):773–785
[18] Derby B (2012) Printing and prototyping of tissues and scaffolds. Science 338(6109):921–926
[19] Ngo TD, Kashani A, Imbalzano G, Nguyen KT, Hui D (2018) Additive manufacturing (3d printing): a review of materials, methods, applications and challenges. Compos Part B Eng 143:172–196
[20] Wang X, Jiang M, Zhou Z, Gou J, Hui D (2017) 3d printing of polymer matrix composites: a review and prospective. Compos Part B Eng 110:442–458
[21] Bodkhe S, Ermanni P (2020) 3d printing of multifunctional materials for sensing and actuation: merging piezoelectricity with shape memory. Eur Polym J 132:109738
[22] Tibbits S (2014) 4d printing: multi-material shape change. Arch Des 84(1):116–121
[23] Kuang X, Roach DJ, Wu J, Hamel CM, Ding Z, Wang T, Dunn ML, Qi HJ (2019) Advances in 4d printing: materials and applications. Adv Funct Mater 29(2):1805290
[24] Pingale P, Dawre S, Dhapte-Pawar V, Dhas N, Rajput A (2022) Advances in 4d printing: from stimulation to simulation. Drug Deliv Transl Res, 1–25
[25] Shao L-H, Zhao B, Zhang Q, Xing Y, Zhang K (2020) 4d printing composite with electrically controlled local deformation. Extrem Mech Lett 39:100793
[26] Yang H, Leow WR, Chen X (2018) 3D printing of flexible electronic devices. Wiley Online Library
[27] Zheng Y, Huang X, Chen J, Wu K, Wang J, Zhang X (2021) A review of conductive carbon materials for 3d printing: materials, technologies, properties, and applications. Materials 14(14):3911
[28] Kwok SW, Goh KHH, Tan ZD, Tan STM, Tjiu WW, Soh JY, Ng ZJG, Chan YZ, Hui HK, Goh KEJ (2017) Electrically conductive filament for 3d-printed circuits and sensors. Appl Mater Today 9:167–175
[29] Flowers PF, Reyes C, Ye S, Kim MJ, Wiley BJ (2017) 3d printing electronic components and circuits with conductive thermoplastic filament. Addit Manuf 18:156–163
[30] Marasso SL, Cocuzza M, Bertana V, Perrucci F, Tommasi A, Ferrero S, Scaltrito L, Pirri CF (2018) Pla conductive filament for 3d printed smart sensing applications. Rapid Prototyp J
[31] Pejak Simunec D, Sola A (2022) Emerging research in conductive materials for fused filament fabrication: a critical review. Adv Eng Mater 2101476 (2022)
[32] Khodabakhshi S, Fulvio PF, Andreoli E (2020) Carbon black reborn: structure and chemistry for renewable energy harnessing. Carbon 162:604–649
[33] Donnet J-B (1993) Carbon black: science and technology. CRC Press
[34] Masiuchok O, Iurzhenko M, Kolisnyk R, Mamunya Y, Godzierz M, Demchenko V, Yermolenko D, Shadrin A (2022) Polylactide/carbon black segregated composites for 3d printing of conductive products. Polymers 14(19):4022
[35] Siripongpreda T, Hoven VP, Narupai B, Rodthongku N (2022) Emerging 3d printing based on polymers and nanomaterial additives: enhancement of properties and potential applications. Eur Polym J 111806
[36] Vivaldi F, Sebechlebská T, Vaněčková E, Biagini D, Bonini A, Kolivoška V (2022) Electric conductivity measurements employing 3d printed electrodes and cells. Anal Chimica Acta 1203:339600
[37] Šikula M, Vaněčková E, Hromadová M, Kolivoška V (2023) Spectroelectrochemical sensing of reaction intermediates and products in an affordable fully 3d printed device. Anal Chimica Acta 1267:341379
[38] Muth JT, Vogt DM, Truby RL, Mengüç Y, Kolesky DB, Wood RJ, Lewis JA (2014) Embedded 3d printing of strain sensors within highly stretchable elastomers. Adv Mater 26(36):6307–6312
[39] Tirado-Garcia I, Garcia-Gonzalez D, Garzon-Hernandez S, Rusinek A, Robles G, Martinez-Tarifa J, Arias A (2021) Conductive 3d printed pla composites: on the interplay of mechanical, electrical and thermal behaviours. Compos Struct 265:113744
[40] Roumy L, Touchard F, Marchand D, Truong Hoang TQ, Martinez-Hergueta F (2023) Durability of joule effect of 3d-printed carbon black/pla: electrical fatigue tests and analytical modelling. Int J Fatigue, 107677
[41] Richeton J, Ahzi S, Vecchio K, Jiang F, Adharapurapu R (2006) Influence of temperature and strain rate on the mechanical behavior of three amorphous polymers: characterization and modeling of the compressive yield stress. Int J Solids Struct 43(7–8):2318–2335
[42] Delbart R, Papasavvas A, Robert C, Hoang TQT, Martinez-Hergueta F (2023) An experimental and numerical study

of the mechanical response of 3d printed pla/cb polymers. Compos Struct 319:117156

[43] Narkis M, Ram A, Stein Z (1981) Electrical properties of carbon black filled crosslinked polyethylene. Polym Eng Sci 21(16):1049–1054

[44] Zhang C, Ma C-A, Wang P, Sumita M (2005) Temperature dependence of electrical resistivity for carbon black filled ultra-high molecular weight polyethylene composites prepared by hot compaction. Carbon 43(12):2544–2553

[45] Zhang J, Yang B, Fu F, You F, Dong X, Dai M (2017) Resistivity and its anisotropy characterization of 3d-printed acrylonitrile butadiene styrene copolymer (abs)/carbon black (cb) composites. Appl Sci 7(1):20

[46] Daniel F, Patoary NH, Moore AL, Weiss L, Radadia AD (2018) Temperature-dependent electrical resistance of conductive polylactic acid filament for fused deposition modeling. Int J Adv Manuf Technol 99(5):1215–1224

[47] Beaucage G, Rane S, Schaefer D, Long G, Fischer D (1999) Morphology of polyethylene-carbon black composites. J Polym Sci Part B Polym Phys 37(11):1105–1119

[48] Rieker TP, Hindermann-Bischoff M, Ehrburger-Dolle F (2000) Small-angle x-ray scattering study of the morphology of carbon black mass fractal aggregates in polymeric composites. Langmuir 16(13):5588–5592

[49] Mathew AP, Oksman K, Sain M (2006) The effect of morphology and chemical characteristics of cellulose reinforcements on the crystallinity of polylactic acid. J Appl Polym Sci 101(1):300–310

[50] Harris AM, Lee EC (2008) Improving mechanical performance of injection molded pla by controlling crystallinity. J Appl Polym Sci 107(4):2246–2255

[51] Inácio EM, Lima MCP, Souza DHS, Sirelli L, Dias ML (2018) Crystallization, thermal and mechanical behavior of oligosebacate plasticized poly (lactic acid) films. Polímeros 28:381–388

[52] Kotsilkova R, Ivanov E, Todorov P, Petrova I, Volynets N, Paddubskaya A, Kuzhir P, Uglov V, Biró I, Kertész K et al (2017) Mechanical and electromagnetic properties of 3d printed hot pressed nanocarbon/poly (lactic) acid thin films. J Appl Phys 121(6):064105

[53] Faber K, Badaczewski F, Ruland W, Smarsly BM (2014) Investigation of the microstructure of disordered, non-graphitic carbons by an advanced analysis method for wide-angle x-ray scattering. Zeitschrift für anorganische und allgemeine Chemie 640(15):3107–3117

[54] Saurel D, Segalini J, Jauregui M, Pendashteh A, Daffos B, Simon P, Casas-Cabanas M (2019) A saxs outlook on disordered carbonaceous materials for electrochemical energy storage. Energy Stor Mater 21:162–173

[55] Gundlach N, Hentschke R (2018) Modelling filler dispersion in elastomers: relating filler morphology to interface free energies via saxs and tem simulation studies. Polymers 10(4):446

[56] Beaucage G, Kammler HK, Pratsinis SE (2004) Particle size distributions from small-angle scattering using global scattering functions. J Appl Crystallogr 37(4):523–535

[57] Beaucage G (1995) Approximations leading to a unified exponential/power-law approach to small-angle scattering. J Appl Crystallogr 28(6):717–728

[58] Beaucage G (1996) Small-angle scattering from polymeric mass fractals of arbitrary mass-fractal dimension. J Appl Crystallogr 29(2):134–146

[59] Hammouda B (2010) Analysis of the Beaucage model. J Appl Crystallogr 43(6):1474–1478

[60] Botean A-I (2018) Thermal expansion coefficient determination of polylactic acid using digital image correlation. In: E3S Web of Conferences, vol. 32, p. 01007 (2018). EDP Sciences

[61] Hou H, Yue Y, Liu J, Xi D, Liu S (2023) Numerical simulation and experimental study of the stress formation mechanism of fdm with different printing paths. J Renew Mater 11(1) (2023)

[62] El Moumen A, Tarfaoui M, Lafdi K (2019) Modelling of the temperature and residual stress fields during 3d printing of polymer composites. Int J Adv Manuf Technol 104:1661–1676

[63] Juwhari HK, Abuobaid A, Zihlif AM, Elimat ZM (2017) Investigation of thermal and electrical properties for conductive polymer composites. J Electron Mater 46(10):5705–5714

[64] Hou YH, Zhang MQ, Rong MZ (2004) Thermally induced performance decay in conductive polymer composites. Polym Compos 25(3):270–279

[65] Zhang J, Yan D-X, Xu J-Z, Huang H-D, Lei J, Li Z-M (2012) Highly crystallized poly (lactic acid) under high pressure. AIP Adv 2(4):042159

[66] Xia H, Lu J, Dabiri S, Tryggvason G (2018) Fully resolved numerical simulations of fused deposition modeling. part i: fluid flow. Rapid Prototyp J

[67] Rieker TP, Misono S, Ehrburger-Dolle F (1999) Small-angle x-ray scattering from carbon blacks: crossover between the fractal and porod regimes. Langmuir 15(4):914–917

[68] Hopkins AR, Reynolds JR (2000) Crystallization driven formation of conducting polymer networks in polymer blends. Macromolecules 33(14):5221–5226

[69] Bao Y, Xu L, Pang H, Yan D-X, Chen C, Zhang W-Q, Tang J-H, Li Z-M (2013) Preparation and properties of carbon black/polymer composites with segregated and double-percolated network structures. J Mater Sci 48:4892–4898

[70] Shi Y-D, Lei M, Chen Y-F, Zhang K, Zeng J-B, Wang M (2017) Ultralow percolation threshold in poly (l-lactide)/poly (ε-caprolactone)/multiwall carbon nanotubes composites with a segregated electrically conductive network. J Phys Chem C 121(5):3087–3098

[71] Jing X, Zhao W, Lan L (2000) The effect of particle size on electric conducting percolation threshold in polymer/conducting particle composites. J Mater Sci Lett 19(5):377–379

[72] Zhao S, Li G, Liu H, Dai K, Zheng G, Yan X, Liu C, Chen J, Shen C, Guo Z (2017) Positive temperature coefficient (ptc) evolution of segregated structural conductive polypropylene nanocomposites with visually traceable carbon black conductive network. Adv Mater Interfaces 4(17):1700265

[73] Wu G, Asai S, Sumita M (2002) Carbon black as a self-diagnosing probe to trace polymer dynamics in highly filled compositions. Macromolecules 35(5):1708–1713